Check for updates

Magnetic molecularly imprinted polymers for efficient solid-phase extraction and HPLC analysis of myricetin in pomegranate pomace

Resalat Yimin, [ID] [a] Zulihumaer Aimaiti,[b] Erkin Tursun*[b] and Maimaiti Tuerxun*[a]

Molecularly imprinted polymers (MIPs) show great promise for the targeted identification of active components in complex mixtures. Nevertheless, the intentional use of MIPs for the accurate extraction of bioactive phytochemicals from neglected fruit processing byproducts is a new area of exploration in sustainable biorefinery practices. In this study, a magnetic molecularly imprinted polymer (Fe_3O_4–NH_2@MIP) was synthesized utilizing a surface imprinting technique on the amino-functionalized magnetic iron trioxide (Fe_3O_4–NH_2) to improve selectivity and separation efficiency for the extraction of myricetin in pomegranate pomace. The polymerization process was successful when the ratio of myricetin, acrylamide (AM), and ethylene glycol dimethacrylate (EGDMA) was established at 1 : 4 : 20. A series of characterizations were performed to validate the successful synthesis, morphology, structural properties, and magnetic strength of the materials. The super-magnetic Fe_3O_4–NH_2@MIP demonstrated significant adsorption capacity and stability. The adsorption behavior of Fe_3O_4–NH_2@MIP for myricetin was effectively characterized by the Langmuir isotherm model and the Pseudo-second order kinetic model. Additionally, these materials were employed for the extraction and quantification of myricetin in pomegranate pomace under optimal conditions. The experimental results indicate that the adsorption capacity of Fe_3O_4–NH_2@MIP was up to 19.10 μg mg^{-1} under the best conditions, with an adsorption time of 60 minutes and a myricetin concentration of 100 μg mL^{-1}. Fe_3O_4–NH_2@MIP posses high selectivity for myricetin compared to rutin and resveratrol, the adsorption capacity was up to 18.8 μg mg^{-1}, 4.1 μg mg^{-1} and 3.7 μg mg^{-1}, respectively. And the content of myricetin in the pomegranate pomace was calculated to be 5.01 μg g^{-1}. The findings indicate that the proposed methodology serves as a viable alternative for the selective quantification of myricetin in samples characterized by complex matrices.

1. Introduction

Pomegranate (*Punica granatum* L.), also known as the "Jewel of winter", is a deciduous shrub belonging to the Lythraceae family,[1] and native to the Middle East, now grown in the Mediterranean, China, India, South Africa, and the United States.[2] The fruit possesses significant economic, nutritional, medicinal, and ornamental attributes, and is highly esteemed across industrial, cultural, and ecological domains.[3] The use of different components of the pomegranate fruit, including the pulp, peel, seeds, flowers, and leaves, is experiencing a notable increase in various industries.[4] Pomegranate is a polyphenol-rich food and medicinal plant containing

flavonols, anthocyanins, tannins, alkaloids, organic acids, proteins, various amino acids, essential trace elements, and multiple vitamins.[5,6] Initial findings suggest that pomegranate has antioxidant, anti-aging, vascular softening, cholesterol-lowering, and other beneficial effects widely utilized in the medical industry.[7] However, the leftovers of pomegranate remaining after extracting pomegranate juice were directly discarded and have not been effectively utilized. The residue of the pomegranate contains a variety of bioactive substances needed for the biological activity, including phenolic acids, minerals, flavonoids, and hydrolyzable tannins.[2] Myricetin is a polyhydroxy flavonoid with hydroxyl substitutions at the 3, 5, 7, 3′, 4′, and 5′ positions[8] that is widespread among natural foods, including teas, beans, berries, propolis, vegetables, pomegranates, grapes, red wine, and medicinal herbs[9] (Fig. 1). Myricetin has received widespread attention due to its diverse biological activities, nutraceutical properties, and health benefits, including anti-inflammatory,[10] antioxidative properties,[11,12] anti-tumor,[13–15] neuroprotective,[16,17] liver protection.[18] Some researchers suggest that myricetin might be a promising

*a*Xinjiang Key Laboratory of Novel Functional Materials Chemistry, College of Chemistry and Environmental Sciences, Kashi University, Kashi 844000, PR China. E-mail: 1729445286@qq.com

*b*Laboratory of Xinjiang Native Medicinal and Edible Plant Resources Chemistry, College of Chemistry and Environmental Sciences, Kashi University, Kashi 844000, PR China. E-mail: erkin0998@163.com
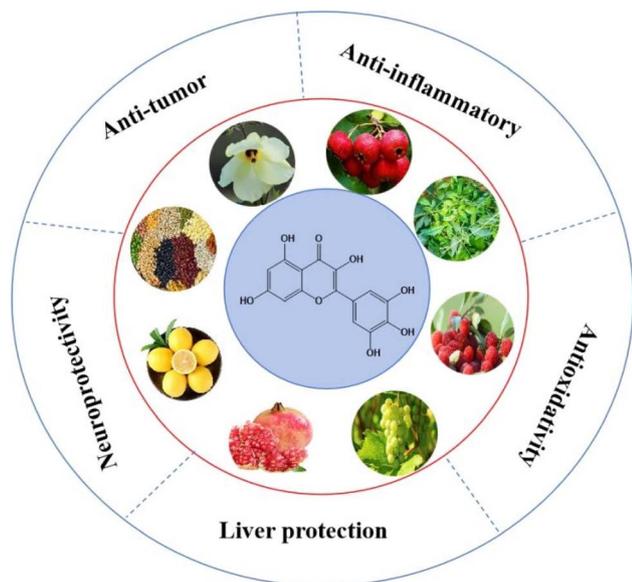
Fig. 1 Structure, sources and biological activity diagram of myricetin.

COVID-19 therapeutic option.[19] Myricetin has been used in food, cosmetics, and beverages in some countries. The estimated intake of myricetin has been reported to be 1.1 mg per day for males and 0.98 mg per day for females.[20] So, it is extremely important to develop simple, efficient, selective, and rapid sample pretreatment and analytical methods to enrich and detect natively occurring myricetin-a pharmaceutically potent flavonoid with demonstrated antioxidative and anti-inflammatory bioactivities-from chemically complex agro-industrial waste matrices.

Molecular imprinting technology (MIT) is a polymerization technique that provides specific recognition and binding abilities to the target molecules.[21,22] MIT enables the prepared polymers to form a special "memory" of the target molecule in terms of spatial structure and functional groups. This allows them to selectively extract target molecules from their analogues in complex samples.[23,24] MIPs based on MIT are utilized as adsorbents and sensors for enriching, separating, purifying, and detecting bioactive components in plants. The advantages, such as high stability and good selectivity make MIPs to be the preferred materials for natural product separation, drug release, chemical and biosensors, solid-phase extraction, environmental applications, catalysis, and other fields.[25–27] However, traditional methods for preparing MIPs still face many limitations in their application to plant natural products due to the high degree of cross-linking. This makes it difficult to elute template molecules and results in a slow mass transfer rate. The occurrence of magnetic core–shell structured nanocomposites has solved the problems mentioned above.[28–30] Magnetic core–shell structured nanocomposites offer the advantages of carriers and molecular imprinting layers, respectively. So, they have the advantages of high recovery rate, simple operation process, and fast separation speed compared to traditional separation technologies such as precipitation and filtration.[31,32]

To the best of our knowledge, there have been no reports on the preparation of magnetic molecularly imprinted polymers for enriching and detecting myricetin in natural plants. In this work, a novel core–shell magnetic molecularly imprinted polymer was prepared on the surface of amino functionalized magnetic iron trioxide ($Fe_3O_4–NH_2$) via surface imprinting method. And this material was applied to enrich and detect myricetin in pomegranate pomace after extracting juice. That can enhance the economic utilization rate of pomegranate pomaces.

2. Materials and methods

2.1 Materials

The pomegranate was purchased from the local bazar. Ferric chloride hexahydrate ($FeCl_3·6H_2O$, AR), anhydrous sodium acetate (NaAc, AR), chromatographic grade methanol (MeOH, AR) were purchased from Xinke Reagent Company (Kashi, China). 1,6-hexanediamine (99%), ethylene glycol (EG, 99.7%), myricetin (HPLC ≥98%), azobisisobutyronitrile (AIBN, 99%), ethylene glycol dimethyl acrylate (EGDMA, 98%), acrylamide (AM, 99%) and methacrylic acid (MAA) were purchased from Macklin Biochemical Technology Co., Ltd (Shanghai, China). Deionized water was used to prepare all solutions required for the experiment.

2.2 Instruments

Scanning electron microscope (SEM, SU8010, HITACHI, Japan) and transmission electron microscopy (TEM, Tecnai F20, FEI, America) were applied to observe the microstructure. X-ray diffractometer (XRD, D8 Advance, BRUKER, Germany) was used for analyzing crystal structure. FT-IR spectrometer (FTIR-200, Hitachi, Japan) was used to scan and determine the functional groups contained in the materials in the wave-number range of 4000–400 cm^{-1}. The magnetic properties of the materials were conducted by the vibrating sample magnetometer (VSM, LakeShore, 7404, America). The thermo gravimetric analysis were performed using a thermal gravimetric analyzer (TGA, NETZSCH, TG 209 F3, Germany) under air from 30 °C to 800 °C at a ramp rate of 10 °C min^{-1}. HPLC analysis was performed on LC-20AT HPLC system with a DAD detector and a AquaSil C18 column (4.6 × 250 mm, 5 μm, Thermo, America).

2.3 Preparation of materials

2.3.1 Synthesis of $Fe_3O_4–NH_2$ particles. $Fe_3O_4–NH_2$ was synthesized by according to a previous method[33] and our team's previous work.[34] Briefly, 1.35 g of $FeCl_3·6H_2O$ was dissolved in 50 mL of ethylene glycol and subjected to ultrasonic treatment for a duration of 30 minutes, resulting in a clear yellow solution. Subsequently, 2.70 g of anhydrous sodium acetate and 17.2 mL of hexanediamine were introduced into the aforementioned solution. The mixture was subjected to mechanical stirring for a duration of 30 minutes before being transferred to a 100 mL Teflon-lined autoclave, where it underwent a reaction at 200 °C for 6 hours. Upon completion of the reaction, the black solid compound isolated was by an external magnet, the compound

was washed with deionized water and anhydrous ethanol to eliminate unreacted reagents and enhance purity. Finally, the compound was dried at 50 °C for 12 hours under vacuum conditions.

2.3.2 Synthesis of Fe₃O₄–NH₂@MIPs/NIPs. The Fe₃O₄–NH₂@MIPs were synthesized through a surface molecular imprinting technique utilizing a one-step polymerization approach. To determine the optimal preparation conditions, various functional monomers (AM and MAA), different ratios of the template molecule, functional monomer, and cross-linker (1 : 4 : 20, 1 : 6 : 30, 1 : 8 : 40), varying amounts of Fe₃O₄–NH₂ (50 mg, 75 mg, 100 mg), and different types of solvents (MeOH and a mixture of MeOH and ACN) were systematically examined. The optimal methodology for the preparation of Fe₃O₄–NH₂@MIP is illustrated in Fig. 2. In summary, 100.0 mg Fe₃O₄–NH₂ (magnetic carrier), 31.8 mg of myricetin (template molecule), 28.4 mg AM, 10 mg AIBN (initiator) and 0.4 mL EDGMA were dissolved into 15 mL of MeOH + ACN (1 : 2, v/v). Subsequently, the mixture underwent ultrasonic treatment for a duration of 10 minutes, followed by the introduction of nitrogen gas for an additional 20 minutes. It was then positioned in a water bath oscillator maintained at a constant temperature, where polymerization occurred at 60 °C for a period of 24 hours. Upon completion of the polymerization reaction, the resulting polymer was isolated using an external magnet. It was subsequently washed three times with methanol and dried in a vacuum dryer at 50 °C for a duration of 10 hours. The Fe₃O₄–NH₂@MIP composite was then subjected to a Soxhlet extraction process to eliminate the template and unreacted reagents, utilizing a mixed solvent of methanol and acetic acid in a volume ratio of 9 : 1. This extraction continued until high-performance liquid chromatography (HPLC) analysis indicated the absence of myricetin. Finally, the material was dried in a vacuum dryer at 50 °C for 24 hours.

As the control group, to evaluate the specificity of the Fe₃O₄–NH₂@MIP's binding sites by comparing adsorption behaviors between imprinted and non-imprinted polymers. Fe₃O₄–NH₂@NIP (non-imprinted polymer) was synthesized without adding myricetin and keeping the polymerization ratio of other raw materials and polymerization conditions consistent with the preparation method of Fe₃O₄–NH₂@MIP.

2.4 Binding experiment

2.4.1 Dynamic adsorption experiment. To assess the kinetics of adsorption, a quantity of 5 mg of Fe₃O₄–NH₂@MIP and Fe₃O₄–NH₂@NIP was introduced into 5 mL of a 20 µg mL⁻¹ myricetin solution, respectively. Followed by agitation for a duration ranging from 5 to 200 minutes. Subsequently, the adsorbents were isolated using an external magnet, and the supernatant was subjected to filtration through a 0.22 µm filter membrane. The resulting solution was then analyzed *via* HPLC at a wavelength of 254 nm. The adsorption capacity of the Fe₃O₄–NH₂@MIP and Fe₃O₄–NH₂@NIP was determined using the following equation:[35]

$$q_e = \frac{(c_o - c_e)V}{m} \qquad (1)$$

where, q_e (µg mg⁻¹) represents the equilibrium adsorption capacity of absorbents for myricetin; c_o (µg mL⁻¹), c_e (µg mL⁻¹) denote the initial and equilibrium concentration of the myricetin solution, respectively; V (mL) stands for the volume of the myricetin solution, and m (mg) represents the mass of absorbents.

Pseudo-first-order (2) and pseudo-second-order (3) kinetic models were employed to investigate the mass transfer mechanisms involved in the adsorption process.[36]

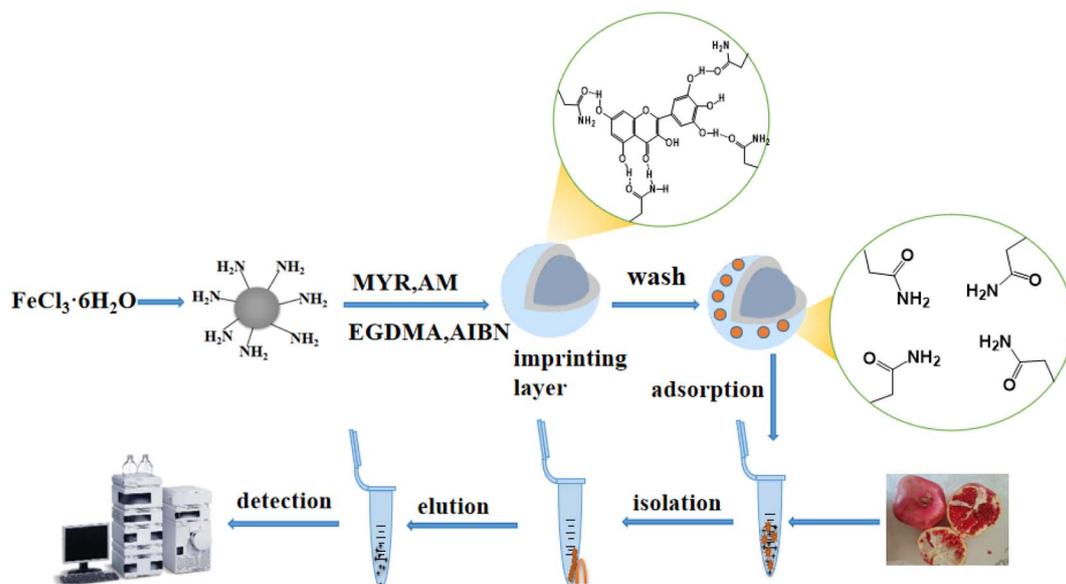$$\lg(q_e - q_t) = \lg q_e - \frac{k_1}{2.303}t \qquad (2)$$

Fig. 2 Synthesis and application process of Fe₃O₄–NH₂@MIP.

$$\frac{t}{q_t} = \frac{t}{q_e} + \frac{1}{k_2 q_e^2} \qquad (3)$$

where, k_1 (min^{-1}), k_2 (mg µg^{-1} min^{-1}) are the reaction rate constants for the pseudo-first-order and pseudo-second-order models, respectively. q_t (µg mg^{-1}) represent the adsorption capacity at a specific time.

2.4.2 Static adsorption experiment. In order to assess the adsorption characteristics of Fe$_3$O$_4$–NH$_2$@MIP and Fe$_3$O$_4$–NH$_2$@NIP, a series of experiments were conducted in which 5 mg of each adsorbent was introduced into 5 mL of myricetin solutions at varying concentrations ranging from 10 to 100 µg mL^{-1}. The subsequent procedures followed the methodology outlined in section 2.4.1.

The Langmuir (4) and Freundlich (5) isothermal adsorption models were utilized to elucidate the adsorption mechanism of myricetin on Fe$_3$O$_4$–NH$_2$@MIP and Fe$_3$O$_4$–NH$_2$@NIP. The corresponding equations are presented below.[37]

$$\frac{c_e}{q_e} = \frac{1}{q_m} c_e + \frac{1}{q_m k_L} \qquad (4)$$

$$\ln q_e = m \ln c_e + \ln k_F \qquad (5)$$

where k_L (mL mg^{-1}) is the Langmuir constant, q_m (µg mg^{-1}) is the maximum adsorption capacity; k_F (µg (mL$^{1/1-n}$ mg)$^{-1}$) is the Freundlich constant related to adsorption capacity, n is an empirical parameter related to adsorption strength.[38]

2.4.3 Selectivity experiment. Selective tests were carried out with myricetin, rutin, resveratrol to assess the specific identification ability of Fe$_3$O$_4$–NH$_2$@MIPs for myricetin and structural analogs. 5 mg of Fe$_3$O$_4$–NH$_2$@MIP or Fe$_3$O$_4$–NH$_2$@NIP was added to 5 mL of a mixed solution of myricetin, rutin, and resveratrol. Then, shaken for 60 min at room temperature. The adsorbents were separated by external magnet, and the supernatant was filtered through a 0.22 µm filter membrane and evaluated using HPLC. The selective adsorption capacity of Fe$_3$O$_4$–NH$_2$@MIP for myricetin was calculated according to eqn (1).

2.5 Application of Fe$_3$O$_4$–NH$_2$@MIP for pomegranate pomace

2.5.1 Sample preparation. A total of 25 grams of dried pomegranate pomace powder underwent extraction through ultrasonication three times, utilizing 250 mL of 80% ethanol at a temperature of 30 °C for a duration of 30 minutes per extraction. Following the extraction process, the resulting solutions were filtered and subsequently combined. The combined extract was then concentrated using a rotary evaporator.

2.5.2 Application of Fe$_3$O$_4$–NH$_2$@MIP to real samples. The pomegranate pomace extracts subjected to Fe$_3$O$_4$–NH$_2$@MIP were comparatively analyzed via HPLC to evaluate the adsorption efficacy, with chromatographic profiles acquired for both pre-adsorption and post-adsorption phases.

2.6 HPLC analysis

HPLC analysis was conducted using an LC-20AT HPLC system equipped with a DAD detector and an AquaSil C18 column (4.6

× 250 mm, 5 µm). The mobile phase A consists of a 0.2% formic acid aqueous solution, while mobile phase B is a 0.1% formic acid solution in acetonitrile. The gradient elution process was as follows: from 0 to 30 minutes, mobile phase A was decreased from 85% to 60%, while mobile phase B increased from 15% to 40%. From 30 to 40 minutes, mobile phase A was held at 60%, and mobile phase B remained at 40%. All sections of the column were maintained at a constant temperature of 30 °C, with an injection volume of 10 µL and a flow rate of 1 mL min^{-1}. The detection wavelength was set at 254 nm.

2.7 HPLC-MS conditions

An UPLC (H-class) coupled with MS (5600 QTOF) method for detecting components in positive and negative ion modes, with A 1.8 µm, 2.1 × 100 mm ACQUITY UPLC HSS T Column (Waters) was applied at a flow rate 400 µL min^{-1}. The same mobile phase and elution program were used in both HPLC and MS systems. Mobile phase A is 0.1% formic acid aqueous solution, mobile phase B is a 0.1% formic acid solution in acetonitrile. The gradient elution process was as follows: 0–1.5 min: A is 95%, B is 5%; 1.5–2.5 min: A is from 95% to 90%, B is from 5% to 10%; 2.5–14 min, A is from 90% to 60%, B is from 10% to 40%; 14–24 min: A is from 60% to 5%, B is from 40% to 95%; 24–27 min: A is 5%, B is 95%; 27–80 min: A is from 5% to 95%, B is from 95% to 5%. All sections of the column were maintained at a constant temperature of 40 °C, with an injection volume of 4 µL. The MS (AB 5600 Triple TOF) was operated under the control Analyst TF 1.7 (AB Sciex) to perform MS1, MS2 data acquisition via IDA functionality. During each acquisition cycle, the most intense precursor ions with signal intensities exceeding 100 were dynamically selected for subsequent MS2 fragmentation and data collection. The MS1 mass range was set to 50–1200 Da with a collision energy of 30 eV. In each acquisition cycle, the top 15 most intense ions were dynamically selected for MS2 fragmentation. Electrospray ionization (ESI) source parameters were optimized as follows: Nebulizer gas (GS1): 60 psi; Auxiliary gas: 60 psi; Curtain gas: 35 psi; Source temperature: 550 °C; Ion spray voltage: 5500 V (positive mode) or −4500 V (negative mode).

3. Results and discussion

3.1 Characterizations results

The samples were directly adhered to conductive adhesive and underwent gold sputtering to enhance their surface conductivity. Their surface morphology and structural characteristics were analyzed using SEM. For TEM analysis, the samples were dispersed in ethanol through ultrasonication for 15 minutes to ensure uniformity. A drop of the resulting suspension was placed on a copper mesh microgrid and allowed to dry, forming a thin film. The samples were examined at an accelerating voltage of 200 kV to evaluate their morphology, structural features, and polymerization behavior. The SEM and TEM images of Fe$_3$O$_4$–NH$_2$ (a and c) and Fe$_3$O$_4$–NH$_2$@MIP (b and d) are presented in Fig. 3. It is evident that the uniformly sized spherical Fe$_3$O$_4$–NH$_2$ particles (100–130 nm) have been
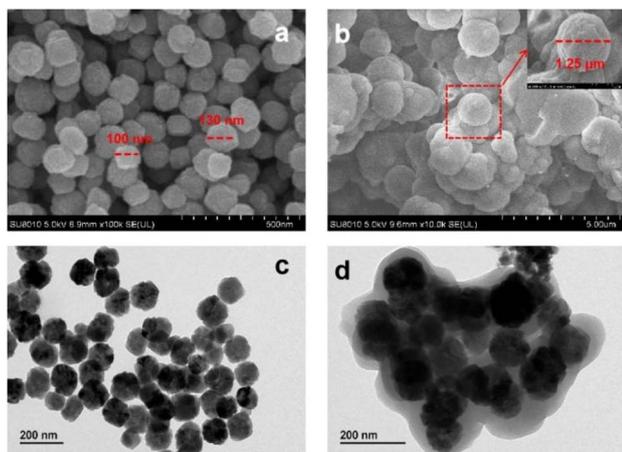
Fig. 3 SEM and TEM images of $Fe_3O_4-NH_2$ (a and c), $Fe_3O_4-NH_2@MIP$ (b and d).

Fig. 5 XRD patterns of $Fe_3O_4-NH_2$ (a), $Fe_3O_4-NH_2@MIP$ (b) and $Fe_3O_4-NH_2@NIP$ (c).

effectively coated with a molecularly imprinted layer, increasing their size to approximately 1.25 μm. A polymerization layer is distinctly visible on the outer surface of $Fe_3O_4-NH_2$, confirming successful polymerization.

Fig. 4 shows the magnetization curves of $Fe_3O_4-NH_2$, $Fe_3O_4-NH_2@MIP$ and $Fe_3O_4-NH_2@NIP$. The materials exhibit no apparent hysteresis, remanence, or coercivity in the loops, indicating good superparamagnetism. The saturation magnetization of $Fe_3O_4-NH_2$ nanoparticles is 62.96 emu g^{-1}. However, after the polymerization reaction on the surface of $Fe_3O_4-NH_2$, the magnetism of $Fe_3O_4-NH_2@MIP$ and $Fe_3O_4-NH_2@NIP$ decreased to 11.62 emu g^{-1} and 7.20 emu g^{-1} due to the barrier effect of the imprinted layer. However, it is still considerably strong, enabling the material to easily separate from the complex in 15 seconds under the action of an external magnet, thus improve material separation efficiency without relying on conventional techniques including centrifugation, filtration, and vacuum filtration.
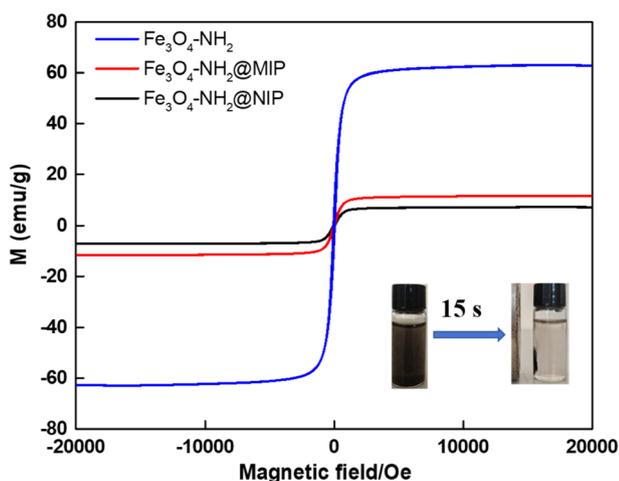
X-ray diffraction was utilized to examine the crystal structure of $Fe_3O_4-NH_2$, $Fe_3O_4-NH_2@MIP$ and $Fe_3O_4-NH_2@NIP$. As shown in Fig. 5, sharp characteristic diffraction peaks are clearly visible at 30.11°, 35.43°, 43.01°, 53.37°, 56.96°, and 62.51°, corresponding to the characteristic diffraction peaks (220), (311), (400), (422), (511), and (440), respectively. This proves the existence of magnetic ions in all composite materials. The data is consistent with the standard XRD data of Fe_3O_4.[39] It was found that the morphology of $Fe_3O_4-NH_2$ was not significantly altered by the polymerization reaction, only the intensity of the 311 peak was slightly weakened due to the outer polymerization layer. Indicating that the polymerization reaction has no effect on the crystal structure of Fe_3O_4.

Thermogravimetric analysis test under a nitrogen atmosphere was used to investigate the thermal stability of $Fe_3O_4-NH_2$ and $Fe_3O_4-NH_2@MIP$. The thermogravimetric analysis (TGA) curves of $Fe_3O_4-NH_2$ and $Fe_3O_4-NH_2@MIP$ are presented in Fig. 6, illustrating the weight loss from 30 °C to 800 °C.

Fig. 4 VSM curves of $Fe_3O_4-NH_2$, $Fe_3O_4-NH_2@MIP$ and $Fe_3O_4-NH_2@NIP$.
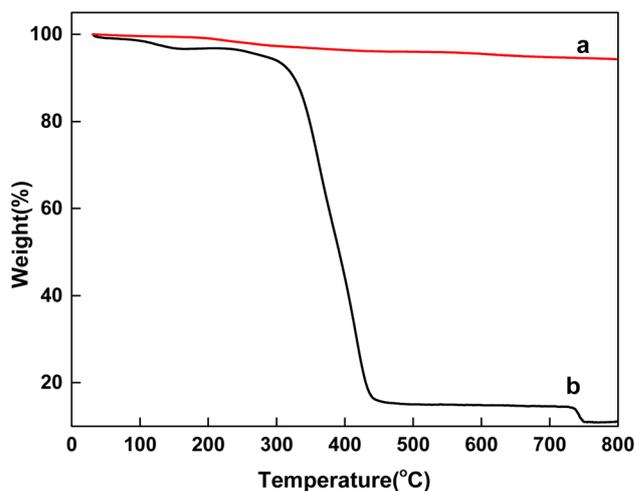
Fig. 6 TGA curves of $Fe_3O_4-NH_2$ (a) and $Fe_3O_4-NH_2@MIP$ (b).
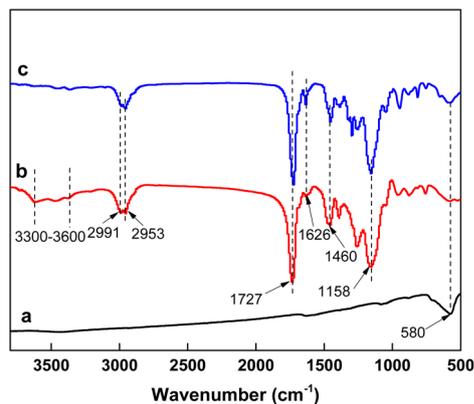
Fig. 7 FTIR spectrum of Fe_3O_4–NH_2 (a), Fe_3O_4–NH_2@MIP (b) and Fe_3O_4–NH_2@NIP (c).

Fe_3O_4–NH_2 began to lose weight by about 1.3% when heated to 234.5 °C due to the amino group on the surface of Fe_3O_4. While Fe_3O_4–NH_2@MIP experienced a weight loss of approximately 5.4% at 125.3 °C, which was attributed to the presence of water and organic reagents, a significant weight loss of 72% was observed when it was heated to 412.4 °C. Which was attributed to the thermal decomposition of the surface-imprinted layer, demonstrating that Fe_3O_4–NH_2@MIP maintains good thermal stability up to 300 °C.

FTIR was applied to verify the structural composition and functional groups present in Fe_3O_4–NH_2 (a), Fe_3O_4–NH_2@MIP (b) and Fe_3O_4–NH_2@NIP (c). The absorption peak at 580 cm^{-1}, as illustrated in Fig. 7, is exclusively associated with the Fe–O stretching vibration in materials,[40] confirming the successful magnetization. The band of high intensity around 1727 cm^{-1} attributes to the stretching vibration of C=O due to EGDMA and myricetin. The peak around 1460 cm^{-1} and 1626 cm^{-1} should be the C=C stretching of the benzene rings and EGDMA. The peak examined at 1158 cm^{-1} is the stretching band of C–O from the EGDMA and myricetin. The peak around 872 cm^{-1} is bending vibration of = C–H in aromatic hydrocarbon, the broad band appeared at about 3300–3600 cm^{-1} is associated with the absorption peak of intermolecular hydrogen bonding between template molecules and functional monomers. These various functional groups are more favorable for the adsorption process.

3.2 Adsorption properties

3.2.1 UPLC-MS analysis of pomegranate pomace.
The total ion chromatogram (TIC) of pomegranate pomace extract obtained via UPLC-MS in both positive and negative ionization modesdemonstrates the remarkable chemical diversity of constituents in the pomace matrix, indicative of a complex phytochemical composition (Fig. 8). Notably, phenylpropanoids
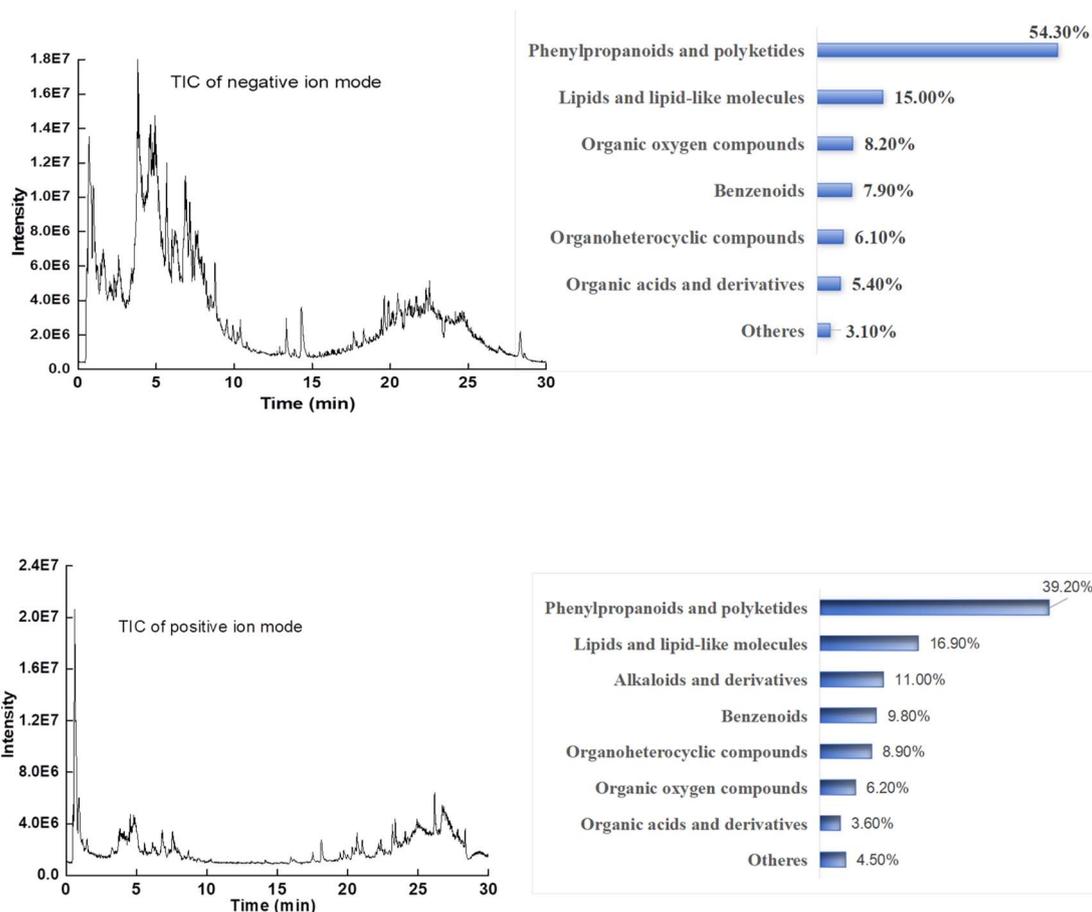

Fig. 8 TIC and constituent content of pomegranate pomace extract.

Table 1 The standard equations and parameters for myricetin, rutin and resveratrol

Name	Regression equation	Linear range ($\mu g \ mL^{-1}$)	R^2	RSD (%)	RSD (%) of stability
Myricetin	$y = 7981.1x - 8962.3$	2.5–80	0.999	1.61	2.31
Rutin	$y = 6323.5x - 42452.3$	10–80	0.999	2.13	2.06
Resveratrol	$y = 3524.8x + 544.4$	0.5–80	0.998	2.42	1.97

and polyketides dominated the phytochemical profile, constituting 54.30% of detectable compounds in negative ion mode and 39.20% in positive mode. This class, encompassing ellagitannins and hydrolyzable tannins characteristic of pomegranates, displayed significant ionization mode-dependent detection efficiency (Δ15.10%). Key compositional differences between negative and positive ion modes included lipid-like molecules (15.00% *vs.* 16.90%), benzenoids (7.90% *vs.* 9.80%), organic oxygen compounds (8.20% *vs.* 6.20%), organic acids and derivatives (5.40% *vs.* 3.60%). Also, negative mode specificity elevated detection of Organoheterocyclic compounds (6.10% *vs.* undetected in positive), however positive mode enhanced alkaloid detection (11.00% *vs.* undetected in negative). This dual-polarity approach effectively captured the full phytochemical spectrum, with orthogonal detection modes compensating for ionization bias towards specific compound classes-a critical strategy for comprehensive plant metabolomics.

The cumulative analytical findings substantiate that pomegranate pomace extracts harbor a sophisticated array of bioactive phytochemicals, whose indiscriminate disposal precipitates substantial resource depletion while exacerbating agricultural waste streams. Thereby the valorization of fruit processing residues is critical for transitioning toward waste-to-wealth circular economies.

3.2.2 HPLC conditions and standard curve. The standard equations for myricetin, rutin and resveratrol were depicted in

Table 1, demonstrated a strong linear correlation for myricetin, rutin and resveratrol, with the linear range of the method was from 2.5 to 80 $\mu g \ mL^{-1}$ ($R^2 = 0.999$) for myricetin, from 10 to 80 $\mu g \ mL^{-1}$ ($R^2 = 0.999$) for rutin, and from 0.5 to 80 $\mu g \ mL^{-1}$ ($R^2 = 0.998$) for resveratrol, and RSD for the precision and stability were lower than 3%.

3.2.3 Adsorption kinetics. The adsorption kinetics of $Fe_3O_4–NH_2$@MIP and $Fe_3O_4–NH_2$@NIP were depicted in Fig. 9. It was observed that with an increase in adsorption time, the adsorption capacity exhibited an upward trajectory. Notably, $Fe_3O_4–NH_2$@MIP demonstrated superior adsorption
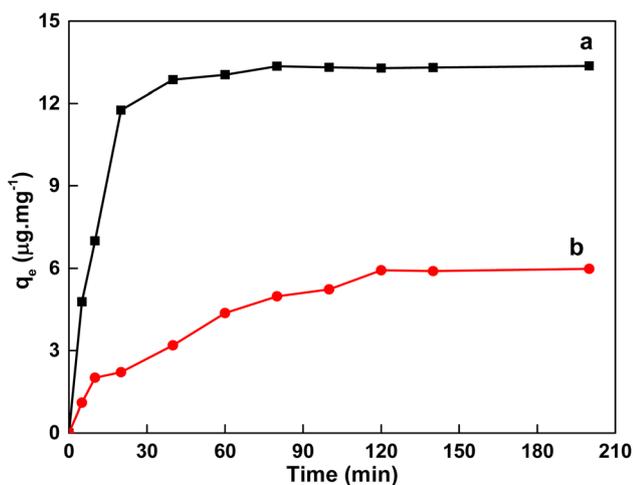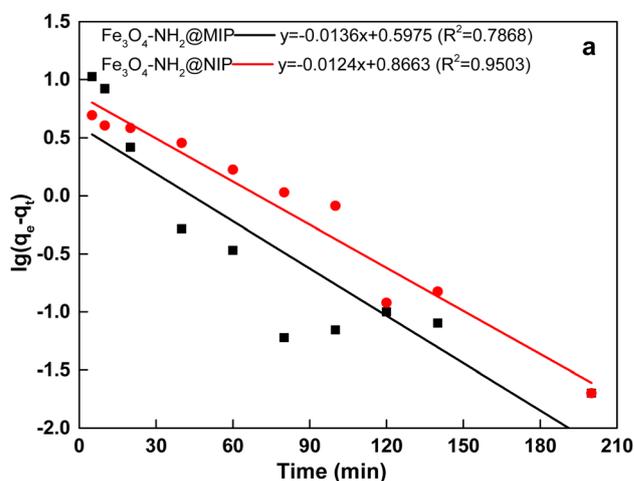

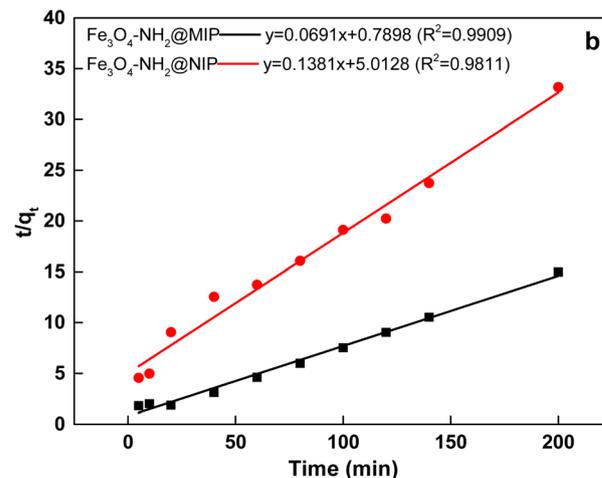**Fig. 9** Kinetic adsorption curves of $Fe_3O_4–NH_2$@MIP (a) and $Fe_3O_4–NH_2$@NIP (b).

Fig. 10 First-order dynamic (a) and pseudo-second-order kinetic model (b) fitting curves.

Table 2 Kinetic parameters of pseudo-first-order, pseudo-second-order

Adsorbent	First order kinetic model				Second order kinetic model				
	k_1 (min^{-1})	$q_{e,cal.}$ (µg mg^{-1})	R_1^2	Δq	k_2 (min^{-1})	$q_{e,cal.}$ (µg mg^{-1})	R_2^2	Δq	v_0
Fe$_3$O$_4$–NH$_2$@MIP	0.0313	3.96	0.7868	−9.41	0.0060	14.47	0.9909	1.11	1.27
Fe$_3$O$_4$–NH$_2$@NIP	0.0286	7.35	0.9503	1.32	0.0038	7.24	0.9811	1.21	0.20

performance for myricetin, with a significant increase in the amount adsorbed occurring within the initial 60 minutes. Subsequently, the adsorption process ultimately approaches equilibrium, as myricetin is initially captured by the imprinted "holes" on the surface of Fe$_3$O$_4$–NH$_2$@MIP, which possess specific recognition capabilities. The surface adsorption mechanism exhibits low mass transfer resistance, facilitating the rapid uptake of myricetin by Fe$_3$O$_4$–NH$_2$@MIP. However, once the imprinted "holes" become saturated, the transfer of myricetin from the surface to the interior of the polymer occurs at a slower rate. This transfer is impeded by resistance, resulting in a gradual decrease in the adsorption rate until it stabilizes, thereby prolonging the time required to achieve saturation.

As shown in Fig. 10 and Table 2, comparing the correlation coefficients ($R^2 = 0.9909$) and the proximity of theoretical adsorption capacity (14.47 µg mg^{-1}) and experimental value (13.36 µg mg^{-1}), the adsorption process of myricetin on Fe$_3$O$_4$–NH$_2$@MIP was well described by the pseudo-second-order kinetic model, indicating that the entire adsorption process is a chemical process and the adsorption rate may be controlled by the interaction between the adsorption site and the template analyte.[39]

3.2.4 Adsorption isotherms. The adsorption isotherms of Fe$_3$O$_4$–NH$_2$@MIP and Fe$_3$O$_4$–NH$_2$@NIP showed in Fig. 11, indicating that the adsorption capacity of Fe$_3$O$_4$–NH$_2$@MIP and Fe$_3$O$_4$–NH$_2$@NIP increased with the increasing of the concentration of the myricetin, it raised fast when the concentration was less than 60 µg mL^{-1}, continuing to increase the concentration of myricetin did not lead to significant increase of the

adsorption capacity, because of the decrease of imprint holes. The large adsorption capacity occurred when the myricetin concentration was 100 µg mL^{-1}, that was up to 19.10 µg mg^{-1}, the results indicating that Fe$_3$O$_4$–NH$_2$@MIP has good adsorption capacity and enrichment efficiency for myricetin, due to the pre-designed hydrogen bonding and π–π stacking.[37]

As shown in Fig. 12 and Table 3, comparing the correlation coefficients ($R^2 = 0.9989$) and the proximity of theoretical adsorption capacity (19.96 µg mg^{-1}) and experimental value (19.10 µg mg^{-1}), the adsorption of myricetin on Fe$_3$O$_4$–NH$_2$@MIP fitted better with the Langmuir model, indicating that the adsorption was mono-molecular layer adsorption, and
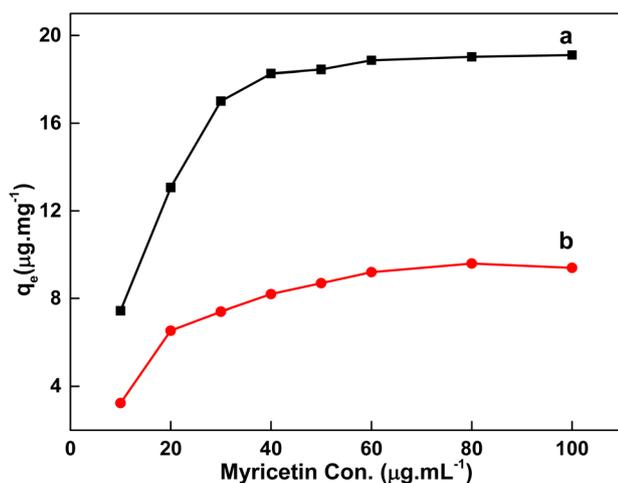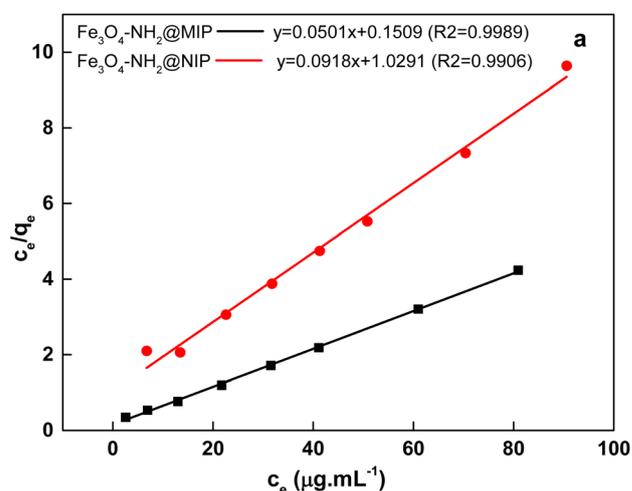

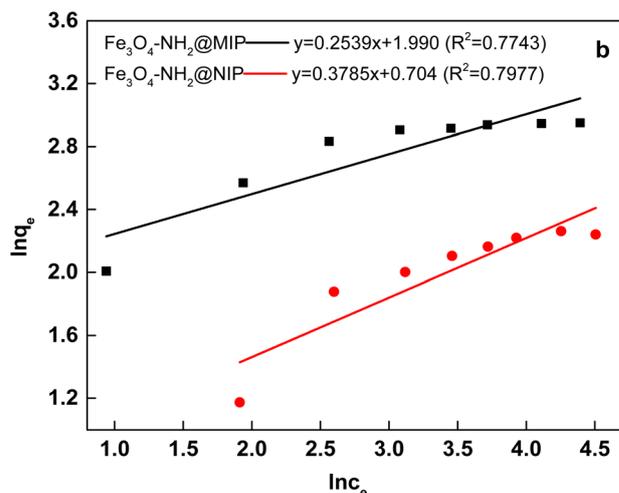Fig. 11 Adsorption isotherms of Fe$_3$O$_4$–NH$_2$@MIP (a) and Fe$_3$O$_4$–NH$_2$@NIP (b).

Fig. 12 Langmuir fitting curves (a) and Freundlich fitting curves (b).

Table 3 Langmuir and Freundlich isotherm model parameters

Adsorbent	Langmuir				Freundlich		
	k_L (mL mg^{-1})	$q_{e,cal.}$ (µg mg^{-1})	R_1^2	Δq	k_F	$1/n$	R_2^2
Fe$_3$O$_4$–NH$_2$@MIP	0.3322	19.96	0.9989	0.86	7.32	0.2539	0.7743
Fe$_3$O$_4$–NH$_2$@NIP	0.0892	10.89	0.9906	1.49	2.02	0.3785	0.7977
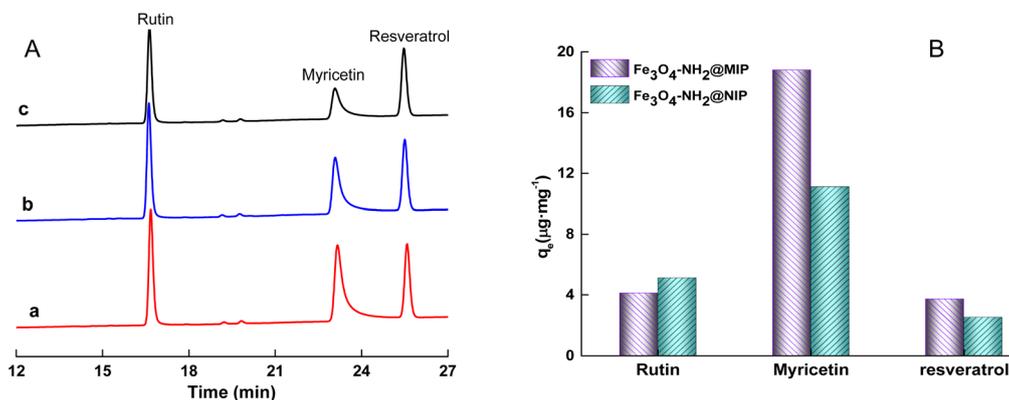
Fig. 13 Adsorption capacity of Fe$_3$O$_4$–NH$_2$@MIP and Fe$_3$O$_4$–NH$_2$@NIP for rutin, myricetin and resveratrol. (a): the initial solution of three compounds; (b) the residual solution of three compounds after adsorption by Fe$_3$O$_4$–NH$_2$@NIP; (c) the residual solution of three compounds after adsorption by Fe$_3$O$_4$–NH$_2$@MIP.

the adsorption sites were distributed on the surface of the adsorbent. Besides that, the value of parameter $1/n$ is between 0 and 1, indicating that the adsorption and removal process was easy carried out.

3.3 Selectivity of Fe$_3$O$_4$–NH$_2$@MIP

As shown in Fig. 13, it was obvious that Fe$_3$O$_4$–NH$_2$@MIP possesses high selectivity for myricetin compared to other two compounds and the adsorption capacity for rutin, myricetin and resveratrol was up to 4.1 µg mg^{-1}, 18.8 µg mg^{-1}, 3.7 µg mg^{-1}. However, the selectivity of Fe$_3$O$_4$–NH$_2$@NIP for myricetin was relatively low. These results indicates that Fe$_3$O$_4$–NH$_2$@MIP had better recognition ability towards myricetin. Revealing that the selective adsorption capacity of Fe$_3$O$_4$–NH$_2$@MIP for myricetin was better than others. In a word, these data indicated Fe$_3$O$_4$–NH$_2$@MIP could use for selective extraction of myricetin from real complex samples.

3.4 Application of Fe$_3$O$_4$–NH$_2$@MIP for pomegranate pomace

Fe$_3$O$_4$–NH$_2$@MIP was used to enrich myricetin contained in pomegranate pomace extract to evaluate the practical applicability. The chromatograms of initial pomegranate pomace extract, the extract after being adsorbed by Fe$_3$O$_4$–NH$_2$@MIP for 60 minutes and 240 minutes were shown in Fig. 14. After adsorption on Fe$_3$O$_4$–NH$_2$@MIP nanoparticles, the peak area of the myricetin was smaller than the peak area of initial sample, while the peak areas of other components did not change significantly, indicating there are imprinting "holes" on the

surface of Fe$_3$O$_4$–NH$_2$@MIP that have specific recognition ability for myricetin. Moreover, the content of myricetin in the pomegranate pomace was calculated to be 5.01 µg g^{-1} using the standard curve $y = 7981.1x - 8962.3$ (2.5–80 µg mL^{-1}, $R^2 = 0.999$), indicating that the Fe$_3$O$_4$–NH$_2$@MIP had the specificity and practicability for the separation of myricetin and can be applied to enrichment of myricetin from complex.
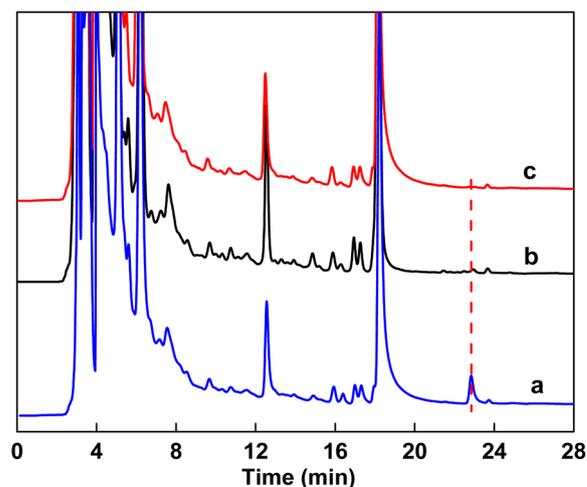

Fig. 14 HPLC of pomegranate peel extract by Fe$_3$O$_4$–NH$_2$@MIP. (a) the HPLC chromatograms of the ethanol extract of pomegranate peel; (b) the HPLC chromatograms of the extract after being adsorbed by Fe$_3$O$_4$–NH$_2$@MIP for 60 min; (c) the HPLC chromatograms of the extract after being adsorbed by Fe$_3$O$_4$–NH$_2$@MIP for 240 min.

4. Conclusions

In conclusion, we have reported the synthesis, characterization, and practical application of Fe_3O_4–NH_2@MIPs with strong magnetic responsiveness, high stability and specific recognition functions. And Fe_3O_4–NH_2@MIPs have been successfully utilized in magnetic solid-phase extraction (MSPE) for the selective enrichment of myricetin in pomegranate pomace with complex compositions. Fe_3O_4–NH_2@MIP has a large adsorption capacity and enrichment efficiency for myricetin due to the pre-designed hydrogen bonding and π–π stacking. Due to the strong magnetic responsiveness, it is easy and quick to separate Fe_3O_4–NH_2@MIP from the solution within 15 seconds using an external magnet, that avoid using time-consuming and energy consuming methods, like centrifugation, filtration, and vacuum filtration. All findings indicate that this material is expected to be the preferred material for separating myricetin during the extraction process.

Data availability

The datasets generated and analysed during this study are included in this published article. This submission represents an authentic study, and the authors affirm that the content has not been previously published and is not currently being reviewed for publication elsewhere.

Author contributions

Resalat Yimin: conceptualization, methodology, writing – original draft. Zulihumaer Aimaiti: data curation, formal analysis. Erkin Tursun: supervision, writing – review & editing. Maimaiti Tuerxun: writing – review & editing.

Conflicts of interest

The authors confirm that they do not have any competing financial interests or personal relationships that could have influenced the findings presented in this paper.

Acknowledgements

References

1 S. Yoon, H. Jeong, S. M. Jo, H. S. Jun, H. Park, Y. Ban, M. Y. Youn and E. C. Shin, Physicochemical and chemosensory properties of pomegranate (*Punica granatum L.*) seeds under various oven-roasting conditions, *Food Chem.*, 2024, **446**, 138907.

2 F. Azmat, M. Safdar, H. Ahmad, M. R. J. Khan, J. Abid, M. S. Naseer, S. Aggarwal, A. Imran, U. Khalid, *et al.*, Phytochemical profile, nutritional composition of pomegranate peel and peel extract as a potential source of nutraceutical: a comprehensive review, *Food Sci. Nutr.*, 2024, **12**, 661–674.

3 J. T. Silva, T. S. Rana, D. Narzary, N. Verma, D. T. Meshram and S. A. Ranade, Pomegranate biology and biotechnology:A review, *Sci. Hortic.*, 2013, **160**, 85–107.

4 G. H. Qin, C. Y. Xu, R. Ming, H. B. Tang, R. Guyot, E. M. Kramer, Y. D. Hu, X. K. Yi, Y. J. Qi, *et al.*, The pomegranate (*Punica granatum L.*) genome and the genomics of punicalagin biosynthesis, *Plant J.*, 2017, **91**, 1108–1128.

5 T. Ismail, S. Akhtar, P. Sestili, M. Riaz, A. Ismail and R. G. Labbe, Antioxidant, Antimicrobial and Urease Inhibitory Activities of Phenolics-Rich Pomegranate Peel Hydro-Alcoholic Extracts, *J. Food Biochem.*, 2016, **40**, 550–558.

6 J. Zhang, L. Li, M. Zhang, X. L. Hu and H. Wang, *Research Progress in Chemical Constituent and Pharmacological Activity of Punica Granatum L.*, Journal of China Pharmaceutical University, 2023, vol. 54, pp. 421–430.

7 M. J. C. Barbosa, F. M. R. Assunção and S. L. A. Lira, Punica granatum leaves as a source of active compounds: A review of biological activities, bioactive compounds, food, and technological application, *Food Biosci.*, 2023, **51**, 102220.

8 L. L. Deng, X. Kang, T. Quan, L. J. Yang, S. C. Liu, K. L. Zhang, M. J. Gao, Z. N. Xia and D. Gao, Highly Crystalline Covalent Organic Frameworks Act as a Dual Functional Fluorescent-Sensing Platform for myricetin and Water, and Adsorbents for myricetin, *ACS Appl. Mater. Interfaces*, 2021, **28**, 33449–33463.

9 W. Xia, B. S. Zheng, T. Li, F. L. Lian, Y. Y. Lin and R. H. Liu, Fabrication, characterization and evaluation of myricetin adsorption onto starch nanoparticles, *Carbohydr. Polym.*, 2020, **250**, 116848.

10 W. Hou, S. Y. Hu, Z. Z. Su, Qi. Wang, G. P. Meng, T. T. Guo, J. Zhang and P. Gao, Myricetin attenuates LPS-induced inflammation in RAW 264.7 macrophages and mouse models, *Future Med. Chem.*, 2018, **19**, 2253–2264.

11 Y. Yao, G. Lin, Y. Xie, P. Ma, Li. Meng and T. Wu, Preformulation studies of myricetin: a natural antioxidant flavonoid, *Pharmazie*, 2014, **69**, 19–26.

12 A. Salimi, Z. Jamali and M. Shabani, Antioxidant Potential and Inhibition of Mitochondrial Permeability Transition Pore by myricetinicetin Reduces Aluminium Phosphide-Induced Cytotoxicity and Mitochondrial Impairments, *Front. Pharmacol.*, 2021, **12**, 719081.

13 L. Chen, T. Fan, M. Wang, C. Y. Zhu, W. Y. Feng, Y. Li and H. M. Yang, a natural inhibitor of CD147, increases sensitivity of cisplatin in ovarian cancer, *Expert Opin. Ther. Targets*, 2024, **28**, 83–95.

14 M. Jiang, M. L. Zhu, L. Wang and S. W. Yu, Anti-tumor effects and associated molecular mechanisms of myricetin, *Biomed. Pharmacother.*, 2019, **120**, 109506.

15 P. A. Phillips, V. Sangwan, D. Borja-Cacho, V. Dudeja, S. M. Vickers and A. K. Saluja, Myricetin induces

pancreatic cancer cell death *via* the induction of apoptosis and inhibition of the phosphatidylinositol 3-kinase (PI3K) signaling pathway, *Cancer Lett.*, 2011, **308**, 181–188.

16 S. Ahmed, H. Khan, M. Aschner, M. M. Hasan and S. T. S. Hassan, Therapeutic potential of naringin in neurological disorders, *Food Chem. Toxicol.*, 2019, **132**, 110646.

17 R. Pluta, S. Januszewski and S. J. Czuczwar, Myricetin as a promising molecule for the treatment of post-ischemic brain neurodegeneration, *Nutrients*, 2021, **13**, 342.

18 C. Guo, G. Q. Xue, B. Pan, M. J. Zhao, S. Chen, J. Gao, T. Chen and L. X. Qiu, Myricetin Ameliorates Ethanol-Induced Lipid Accumulation in Liver Cells by Reducing Fatty Acid Biosynthesis, *Mol. Nutr. Food Res.*, 2019, **63**, 1801393.

19 T. Xiao, M. Cui, C. Zheng, M. Wang, R. Sun, D. Gao and H. Zhou, Myricetin inhibits SARS-CoV-2 viral replication by targeting Mpro and ameliorates pulmonary inflammation, *Front. Pharmacol.*, 2021, **12**, 1012.

20 J. Lin, S. M. Zhang, K. Wu, W. C. Willett, C. S. Fuchs and E. Giovannucci, Flavonoid intake and colorectal cancer risk in men and women, *Am. J. Epidemiol.*, 2006, **164**, 644–651.

21 G. Vasapollo, R. D. Sole, L. Mergola, M. R. Lazzoi, A. Scardino, S. Scorrano and G. Mele, Molecularly Imprinted Polymers: Present and Future Prospective, *Int. J. Mol. Sci.*, 2011, **12**, 5908–5945.

22 C. Y. Dong, H. X. Shi, Y. R. Han, Y. Y. Yang, R. X. Wang and J. Y. Men, Molecularly imprinted polymers by the surface imprinting technique, *Eur. Polym. J.*, 2021, **145**, 110231.

23 J. J. BelBruno, Molecularly Imprinted Polymers, *Chem. Rev.*, 2019, **119**, 94–119.

24 L. X. Chen, X. Y. Wang, W. H. Lu, X. Q. Wua and J. H. Li, Molecular imprinting: perspectives and applications, *Chem. Soc. Rev.*, 2016, **45**, 2137.

25 C. Jantarat, K. Attakitmongkol, S. Nichsapa, P. Sirathanarun and S. Srivaro, Molecularly imprinted bacterial cellulose for sustained-release delivery of quercetin[J], *J. Biomater. Sci. Polym. Ed.*, 2020, **31**, 1961.

26 M. Cantarella, C. C. Sabrina, S. Dattilo, R. Avolio, R. Castaldo, C. Puglisi and V. Privitera, Molecularly imprinted polymer for selective adsorption of diclofenac from contaminated water, *Chem. Eng. J.*, 2019, **367**, 180.

27 Y. Y. Wen, S. C. Zhao, Z. J. Yu, W. W. Gong, S. Y. Lu, H. Y. Li and J. Wang, Preparation of molecularly imprinted polymer for the specific adsorption and selective extraction of alkylresorcinols from whole wheat flour, *Food Chem.*, 2024, **454**, 139815.

28 F. Q. Wang, X. Ni, J. J. Zhang, Q. K. Zhang, H. N. Jia, H. He and P. Dramou, Novel composite nanomaterials based on magnetic molecularly imprinted polymers for selective extraction and determination of rutin in fruit juice, *Food Chem.*, 2022, **381**, 1–8.

29 T. L. Wang, H. Z. Xie, Y. T. Cao, Q. Xu and N. Gan, Magnetic solid phase extraction coupled with high-performance liquid chromatography-diode array detection based on assembled magnetic covalent organic frameworks for selective extraction and detection of microcystins in aquatic foods, *J. Chromatogr. A.*, 2022, **1685**, 463614.

30 H. Y. Wang, S. S. Jiang, Z. X. Xu, S. Zhou and L. H. Xu, A novel fluorescent sensor based on a magnetic covalent organic framework-supported, carbon dot-embedded molecularly imprinted composite for the speciffc optosensing of bisphenol A in foods, *Sens. Actuators, B*, 2022, **361**, 131729.

31 N. Li, D. Wu, J. C. Liu, N. Hu, X. X. Shi, C. J. Dai, Z. W. Sun, Y. R. Suo, G. L. Li and Y. N. Wu, Magnetic covalent organic frameworks based on magnetic solid phase extraction for determination of six steroidal and phenolic endocrine disrupting chemicals in food samples, *Microchem. J.*, 2013, **143**, 350–358.

32 F. Mirzapor and M. Sadeghi, Magnetic molecular imprinted polymers for *in vitro* controlled release and solid-phase extraction of dextromethorphan: synthesize, characterization, and application, *Iran. Polym. J.*, 2022, **31**, 553–571.

33 L. Y. Wang, J. Bao, L. Wang, F. Zhang and Y. D. Li, One-pot synthesis and bioapplication of amine-functionalized magnetite nanoparticles and hollow nanospheres, *Chem. Eur. J.*, 2006, **12**, 6341–6347.

34 R. Yimin, R. Abula and M. Tuerxun, Selective Enrichment of Juglone in Walnut Green Peel Using Core-Shell Magnetic Molecularly Imprinted Polymer, *Food Science*, 2024, **48**, 41–47.

35 Y. Cheng, J. Y. Nie, H. D. Liu, L. X. Kuang and G. F. Xu, Synthesis and characterization of magnetic molecularly imprinted polymers for effective extraction and determination of kaempferol from apple samples, *J. Chromatogr. A.*, 2020, **1630**, 461531.

36 E. Kasiri, H. Haddadi, H. Javadian and A. Asfaram, Highly effective pre-concentration of thymol and carvacrol using nano-sized magnetic molecularly imprinted polymer based on experimental design optimization and their trace determination in summer savoury, Origanum majorana and Origanum vulgare extracts, *J. Chromatogr. B*, 2021, **1182**, 122941.

37 D. L. Xie, Y. Kuang, B. N. Yuan, Y. L. Zhang, C. Y. Ye, Y. Y. Guo, H. Qiu, J. N. Ren, S. O. Alshammari, Q. A. Alshammar, *et al.*, Convenient and highly efficient adsorption of diosmetin from lemon peel by magnetic surface molecularly imprinted polymers, *J. Mater. Sci. Technol.*, 2025, **211**, 159–170.

38 Y. Z. Zhang, B. Qin, B. Zhang, J. G. Ma, Y. Q. Hu, L. Han, M. F. He and C. Y. Liu, Specific enrichment of caffeic acid from Taraxacum mon-golicum Hand.-Mazz. by pH and magnetic dual-responsive molecularly imprinted polymers, *Anal. Chim. Acta*, 2020, **1096**, 193e202.

39 X. H. Li, Y. Y. Cui, X. Wu, A. Abdukayum and C. X. Yang, Fabrication of zwitterionic magnetic microporous organic network for efficient extraction of fluoroquinolone antibiotics from meat samples, *Food Chem.*, 2023, **429**, 136808.

40 M. M. Yu, S. Wang, N. L. Wang, Y. F. Wu, L. R. Li and X. Q. Lu, Magnetic dummy-template molecularly imprinted polymer with an ultrathin shell for selective enrichment of geosmin in water sample, *J. Ind. Eng. Chem.*, 2024, **136**, 349–358.